Eur. Phys. J. A (2021) 57:277
https://doi.org/10.1140/epja/s10050-021-00590-w

THE EUROPEAN PHYSICAL JOURNAL A

Regular Article - Experimental Physics

# Measurement of the $^{232}$Th(n,f) cross section with quasi-monoenergetic neutron beams in the energy range 2–18 MeV

**V. Michalopoulou**[1,2,a], **M. Axiotis**[3], **S. Chasapoglou**[1], **Z. Eleme**[4], **G. Gkatis**[1], **A. Kalamara**[1,5,6], **M. Kokkoris**[1], **A. Lagoyannis**[3], **N. Patronis**[4], **A. Stamatopoulos**[1], **A. Tsantiri**[1], **R. Vlastou**[1]

[1] Department of Physics, National Technical University of Athens, Zografou Campus, Athens, Greece
[2] European Organisation for Nuclear Research (CERN), Geneva, Switzerland
[3] Tandem Accelerator Laboratory, Institute of Nuclear and Particle Physics, N.C.S.R. "Demokritos", Aghia Paraskevi, Athens, Greece
[4] University of Ioannina, Department of Physics, Ioannina, Greece
[5] Institute of Nuclear and Radiological Sciences, Technology, Energy and Safety, N.C.S.R. "Demokritos", Aghia Paraskevi, Athens, Greece
[6] Institute of Nanoscience and Nanotechnology, N.C.S.R. "Demokritos", Aghia Paraskevi, Athens, Greece

Received: 28 July 2021 / Accepted: 16 September 2021 / Published online: 27 September 2021
© The Author(s) 2021, corrected publication 2021
Communicated by Cedric Simenel

**Abstract** The fission cross section of $^{232}$Th has been measured at fast neutron energies, using a setup based on Micromegas detectors. The experiment was performed at the 5.5 MV Van de Graaff Tandem accelerator in the neutron beam facility of the National Centre for Scientific Research "Demokritos". The quasi-monoenergetic neutron beams were produced via the $^{3}$H(p,n), $^{2}$H(d,n) and $^{3}$H(d,n) reactions, while the $^{238}$U(n,f) and $^{235}$U(n,f) reactions were used as references, in order to acquire cross-section data points in the energy range 2–18 MeV. The characterization of the actinide samples was performed via $\alpha$-spectroscopy with a Silicon Surface Barrier (SSB) detector, while Monte Carlo simulations with the FLUKA code were used to achieve the deconvolution of the $^{232}$Th $\alpha$ peak from the $\alpha$ background of its daughter nuclei present in the spectrum. Special attention was given to the study of the parasitic neutrons present in the experimental area, produced via charged particle reactions induced by the particle beam and from neutron scattering. Details on the data analysis and results are presented.

## 1 Introduction

Accurate cross-section data of neutron-induced reactions on actinides are of considerable importance for the design of advanced nuclear systems, such as Generation IV reactors and Accelerator-Driven Systems (ADS). In addition, alternative fuel cycles are investigated, such as the thorium cycle, in order to make the production of energy safer, sustainable, economic and proliferation resistant [1].

Thorium is a naturally occurring material containing almost exclusively the fertile $^{232}$Th isotope and it is 3–4 times more abundant than uranium. In the thorium cycle $^{232}$Th captures a neutron and converts to the fissile $^{233}$U after two consecutive $\beta^-$ decays. The main advantages of the thorium cycle, compared with the conventional uranium cycle, are: the absorption cross section in the thermal region of $^{232}$Th is almost three times higher than the corresponding one of $^{238}$U rendering it possible to achieve a better conversion to the fertile material; the fertile $^{233}$U has a higher neutron yield per neutron absorbed than both $^{235}$U and $^{239}$Pu and thorium oxide is chemically more stable, has a high radiation resistance and does not oxidize any further [2]. On the other hand, the main disadvantage of the thorium cycle is the production of $^{232}$U, with a half-live of 73.6 years, accompanied by its daughters which include strong $\gamma$-ray emitters with very short half-lives. This results in a buildup of the radiation dose, which becomes a problem when storing the spent fuel.

In addition, fission cross-section data are an important part of the study of the fission process. Specifically, narrow resonances and fine structures have been observed in the threshold region of the fission cross section of thorium isotopes, known as the thorium anomaly. Möller and Nix [3] suggested the existence of a triple-humped barrier in order to explain these structures, which is supported by the recent calculations of Sin et al. [4] for the $^{232}$Th and $^{231}$Pa isotopes.

Various experimental datasets for the fission cross section of $^{232}$Th in the energy range covered by the present work are available in EXFOR [5–21], while only the latest data of Shcherbakov et al. and the older data of Lisowski et al. cover the whole fast neutron energy region. Still discrepancies in the order of 30% are observed between the

[a] e-mail: veatriki.michalopoulou@cern.ch (corresponding author)

existing datasets, while the evaluated libraries also present differences up to 10%. In an attempt to resolve these discrepancies and improve the accuracy of the evaluations, data points in the fast neutron energy region are provided, with the use of quasi-monoenergetic neutron beams, produced via different charged particle reactions, in order to cover a wide energy region (from 2.0 to 17.8 MeV). The experimental setup, analysis procedure and Monte Carlo simulations are presented in this work, leading to the determination of the cross section for the $^{232}$Th(n,f) reaction.

## 2 Experimental setup

### 2.1 Neutron sources

The experiment was performed in the neutron beam facility of the National Centre for Scientific Research "Demokritos" using the 5.5 MV Van de Graaff Tandem accelerator. In total twelve irradiations were performed with three different neutron producing reactions, in order to cover the fast neutron energy spectrum.

To cover the energy range from 2.0 to 5.3 MeV the $^{3}$H(p,n) reaction (Q = −0.76 MeV) was used, for neutron energies which correspond to the fission plateau. This reaction was used for the first time for the production of neutrons at "Demokritos" . The solid TiT target was placed in between Mo foils of 10 $\mu$m thickness, where the charged particle beam loses part of its initial energy and a Cu plate of 1 mm thickness, which acts as beam stop. The target assembly was air-cooled during the irradiations. Eight irradiations were performed with proton beams in the energy region 3.4–6.5 MeV, in order to acquire the desired neutron energies.

One irradiation was performed between the first and second chance fission peaks, at 9.9 MeV, while the deuteron beam was 7.0 MeV. The neutrons were produced via the $^{2}$H(d,n) reaction (Q = 3.27 MeV), with the deuteron beam impinging on a deuterium gas target, kept at constant temperature and atmospheric pressure inside the gas cell. The entrance of the gas cell was a 5 $\mu$m thin Mo foil and the beam stop a 1 mm thick Pt one. In order to take into account parasitic reactions of the deuteron beam in the beam line and the gas cell, data were taken with and without the deuterium gas. In addition, the contribution of the deuteron break-up in the deuterium gas was estimated via Monte Carlo simulations (Sect. 3.2).

In the region of the second chance fission and before the peak of the third chance fission, three irradiations were performed. The neutrons were produced via the $^{3}$H(d,n) reaction (Q = 17.6 MeV), using the same TiT target of the $^{3}$H(p,n) irradiations. The deuteron beam energies were 1.8, 2.3 and 2.8 MeV in order to obtain neutron beams of 14.8, 16.5 and 17.8 MeV, respectively. Data were taken with an identical target case to the TiT target, by placing a Cu foil in the position of the target, with the scope of estimating the effect of parasitic reactions of the deuteron beam with the beam line and the target case. The contribution from these parasitic reactions was found to be negligible.

### 2.2 Actinide samples

Two $^{232}$Th samples were used for the measurements, while two $^{238}$U and one $^{235}$U samples were used as references. In addition, a $^{237}$Np sample was used to monitor the parasitic neutrons which accompany the main neutron beam, but it was not used in the analysis of the data. The samples were produced at IPPE (Obninsk) and JINR (Dubna) via the painting technique. The actinide material was deposited on a thin aluminum backing, while the diameter of the deposited area was 8.0 cm for the $^{232}$Th and $^{237}$Np samples and 5.2 cm for the uranium reference samples. Aluminum masks of 4 and 5 cm were placed in front of all samples to define the angular acceptance of the neutron beam and minimize the uncertainty of the neutron beam energy in the samples.

The characterization of the samples was performed via $\alpha$-spectroscopy, with the use of a Silicon Surface Barrier (SSB) detector having a diameter of 6.2 cm. The samples were measured with the aluminum masks used in the experiments. Each sample was placed in a vacuum chamber on top of the SSB detector, so that the surface of the detector was at a distance of ∼0.1 cm from the sample. The solid angle subtended by the detector was estimated via SACALC3 [22], based on the Monte Carlo method, and it was almost equal to $2\pi$. The estimation of the solid angle from the geometric characteristics of the setup introduces a systematic uncertainty of the order of 3% on the calculated mass.

The mass of the samples was estimated via the equation

$$m = \frac{4\pi A_{\Omega}}{\Omega\alpha}, \tag{1}$$

where m is the calculated mass in mg, $A_{\Omega}$ is the activity in the solid angle $\Omega$ subtended by the detector in Bq and $\alpha$ is the specific activity, which corresponds to the activity per unit mass in Bq/mg and is a physical property of the radionuclide.

In the experimental spectrum the $\alpha$ peak which corresponds to the $^{232}$Th sample lies in the tail of the $\alpha$ peaks from the $\alpha$ decays of its daughter nuclides, which are present in the sample. In order to account for the contribution of the daughter nuclides in the $^{232}$Th peak, simulations were performed with the FLUKA code [23,24]. The energies and the intensities of the $\alpha$ particles emitted from each isotope were taken into account in the simulations. The energy deposition in the detector from each nuclide was separately simulated. For the deconvolution of the $\alpha$ peaks, a crystal ball function was assumed for the detector response and chi-square minimization with MINUIT [25] was performed in order to achieve

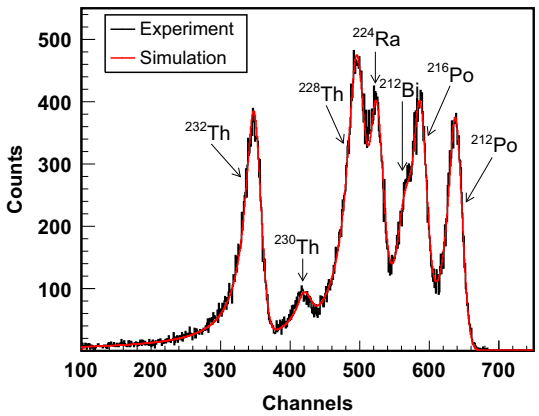


**Fig. 1** Experimental $\alpha$-spectroscopy spectrum (black line) for the $^{232}$Th sample, along with the simulated FLUKA spectrum (red line). The daughter nuclei of $^{232}$Th are present in the spectrum

the optimum agreement between the experimental and simulated spectra. The free parameters used in the minimization was the activity of the nuclides present in the sample, without assuming a priori secular equilibrium between them. Although, the final results did not deviate significantly from the equilibrium state. A typical example of an experimental spectrum in comparison to a simulated one is presented in Fig. 1 and as can seen they are in very good agreement. The same methodology was applied for the calculation of the mass of the uranium reference samples and was found to be in very good agreement with previous $\alpha$-spectroscopy measurements on the same samples with a different methodology [26]. The sample characteristics are presented in Table 1.

### 2.3 Micromegas detectors

The experiment was performed with a setup based on Micro-Bulk Micromegas (Micro-Mesh Gaseous Structure) detectors [28,29]. Each actinide sample was coupled with a Micromegas detector for the detection of the fission fragments. The sample-Micromegas setup was placed in an aluminum chamber filled with Ar:$CO_2$ (90:10) at atmospheric pressure and room temperature. The experimental setup with the aluminum chamber and the end of the beam line, is shown in Fig. 2, while the black and yellow arrows indicate the direction of the charged particle beam and the neutron beam respectively.

The Micromegas is a two region detector, defined by three electrodes: the cathode electrode which is the actinide sample itself, the mesh electrode and the anode electrode. In the cathode electrode a voltage of $\sim$–1 kV is applied, while in mesh electrode a lower voltage of $\sim$–300 V is usually chosen. The anode electrode is grounded through a 50 $\Omega$ resistor. The distance between the cathode and the mesh electrode was chosen for this work to be 8 mm, while the distance

**Table 1** Main characteristics of the actinide samples

| Sample properties | $^{232}$Th (side:1) | $^{232}$Th (side:3) | $^{238}$U (label:209) | $^{238}$U (label:210) | $^{235}$U | $^{237}$Np** |
|---|---|---|---|---|---|---|
| Sample diameter (cm) | 8.0 | 8.0 | 5.2 | 5.2 | 5.2 | 8.0 |
| Sample mask (cm) | 5.0 | 4.0 | 5.0 | 5.0 | 5.2 | 4.0 |
| Mass* (mg) | 5.60 ± 0.02 | 3.47 ± 0.01 | 8.92 ± 0.05 | 8.19 ± 0.05 | 4.98 ± 0.03 | 1.24 ± 0.02 |
| Areal density (x$10^{17}$ nuclei/cm$^2$) | 7.401 ± 0.02 | 7.17 ± 0.03 | 11.5 ± 0.07 | 10.6 ± 0.06 | 6.01 ± 0.03 | 1.57 ± 0.23 |
| Impurities | Nuclides of the $^{232}$Th decay chain | | – | – | $^{234}$U | $^{241}$Am |

*Estimated with the sample mask. **Sample properties taken from [27]

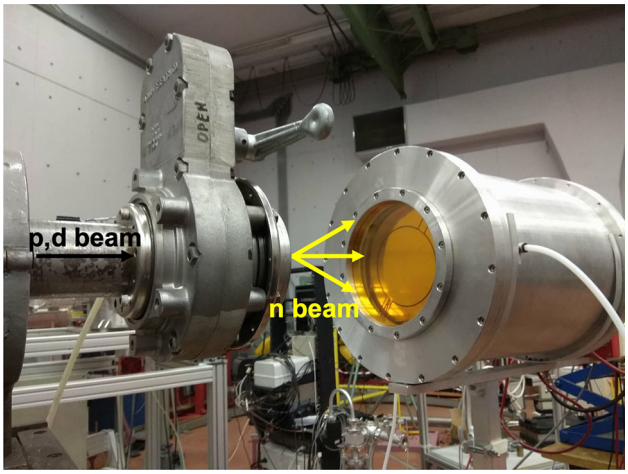


**Fig. 2** The experimental setup used for the measurements. The direction of the particle beam in shown with the black arrow. The neutron beam is created in the target and reaches the aluminum chamber, holding the actinide samples and Micromegas detectors

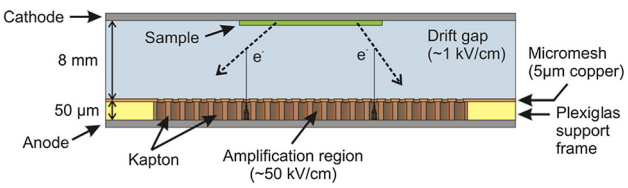


**Fig. 3** Schematic representation of the Micromegas detector [26]

between the mesh and the anode electrode is fixed at 50 $\mu$m. The combination of the voltages applied to the electrodes and their distances define the electric fields created in both regions.

The drift region, between the cathode and the mesh, had an electric field of about 1 kV/cm. The scope of the field is to guide the electrons created from the interaction of the charged particles entering the gas from the drift electrode to pass through the holes present in the mesh electrode. Then a strong field of about 50 kV/cm is present, in order to achieve the multiplication of the electrons through avalanches. The signal is a result of the movement of the charges and is collected from the mesh electrode with a low gain preamplifier, also used for the voltage supply of the electrode. The preamplifier signal was processed using standard spectroscopy amplifiers and passed through ADCs in order to digitally record the signal, in the form of an amplitude spectrum (Fig. 3 [26]).

## 3 Data analysis

The fission cross section of $^{232}$Th, at each neutron energy, was calculated via the expression

$$\sigma(E) = \frac{Y_{Th}(E)}{Y_{ref}(E)} \cdot \frac{\Phi_{ref}(E)}{\Phi_{Th}(E)} \cdot \frac{N_{ref}}{N_{Th}} \cdot \sigma_{ref}(E) \quad (2)$$

where Y are the recorded counts, corrected for the amplitude cut introduced in the analysis in order to discard the $\alpha$ counts, the dead time and the contribution from parasitic neutrons, $\Phi$ is the neutron fluence incident in the position of each sample, $N$ is the areal density of the sample and $\sigma_{ref}$ is the cross section of the reference reaction, while the subscripts "$Th$" and "$ref$" refer to the thorium and reference samples, respectively.

### 3.1 Neutron fluence

Monte Carlo simulations with the MCNP6 code [30] were performed for the determination of the neutron fluence incident on each sample. The simulations were used for the estimation of the ratio $\Phi_{ref}(E)/\Phi_{Th}(E)$ of Eq. (2), which is mainly a geometric correction for the neutron fluence between the thorium and the reference samples, due to the different distances from the neutron source and —in some cases— different diameter mask used in the samples. In addition, the uncertainty of the neutron energy was estimated from the FWHM of the main peak in the simulations.

The description of the neutron source imported in MCNP6 was generated with the NeuSDesc code, coupled with SRIM-2008, taking into account the energy loss of the charged particle beam in the target and the kinematics of each neutron producing reaction. In the case of the $^{2}$H(d,n) reaction the deuteron break-up in the gas-cell was also considered. The aluminum chamber, containing the Micromegas detectors and the actinide samples, and the neutron producing target were described in the input file. The neutron fluence in the position of each sample was the result of the Monte Carlo simulations for all neutron energies.

The neutron fluence estimated from the Monte Carlo simulations for the first $^{232}$Th sample for the irradiations corresponding to neutron energy of 3 MeV (from the $^{3}$H(p,n) reaction), 9.9 MeV (from the $^{2}$H(d,n) reaction) and 17.8 MeV (from the $^{3}$H(d,n) reaction) is presented in Fig. 4. In the 9.9 MeV irradiation, the break-up peak is present in the fluence at approximately 2.5 MeV.

### 3.2 Parasitic neutrons

In addition to the main neutron beam, parasitic neutrons are produced from neutron scattering in the experimental area and the experimental setup and via charged particle reactions of the particle beam with nuclei present in the beam line, the neutron producing target and the experimental setup. In order to acquire accurate results from the measurements it is necessary to take these neutrons into account.

Firstly, the neutrons created from the neutron producing reaction and scattered by the experimental setup materials, including the neutron producing target and the chamber containing the Micromegas detectors and actinide samples, are

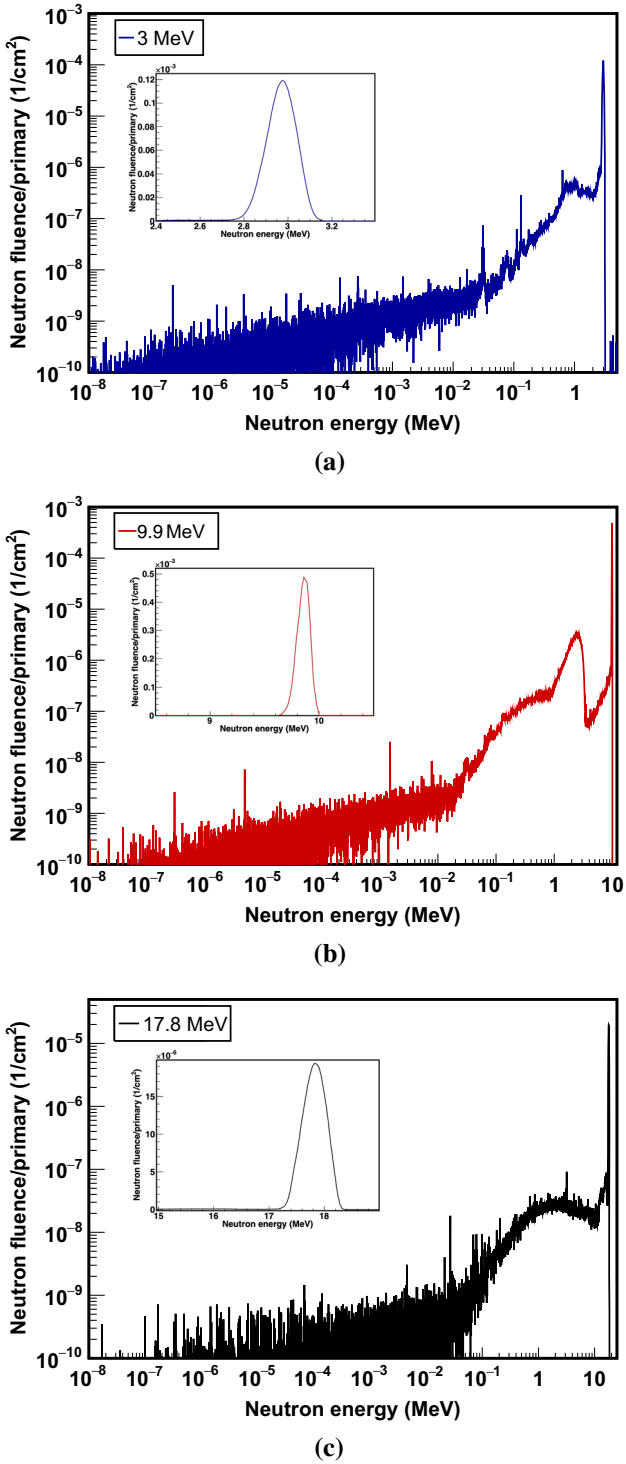


**Fig. 4** Simulated neutron uence from MCNP6 on the $^{232}$Th sample for the irradiations at **a** 3.0, **b** 9.9 and **c** 17.8 MeV performed with the $^{3}$H(p,n), $^{2}$H(d,n) and $^{3}$H(d,n) reactions respectively. The neutron fluence from the main peak for each neutron energy is shown in the insets

included in the Monte Carlo simulations. These form the low neutron tail, as seen in Fig. 4, which begins at the end of the main peak and goes down to the thermal region. In the case of the $^{2}$H(d,n) reaction, the deuteron break-up inside the deuterium gas is also taken into account by the simulations, which is a result of the deuteron beam interacting with the deuterium gas target and it is included as part of the description of the neutron source from the NeuSDesc code. In order to correct for these parasitic counts the methodology described in [26,31] is implemented. The parasitic counts recorded in the experimental amplitude spectra are a result of the parasitic flux in combination with the cross section of each isotope. The correction in the recorded counts for the parasitic neutrons present in the experimental area is estimated from the following expression

$$f_{par} = \frac{\sum_{main} \sigma(E)\Phi(E)}{\sum_{total} \sigma(E)\Phi(E)} \tag{3}$$

where the sum of the numerator corresponds to the integrated reaction rate of the main fluence, while the sum of the denominator corresponds to the total integrated reaction rate. The cross-section values ($\sigma$) were taken from the ENDF/B-VIII.0 evaluation [32], estimated via linear interpolation to correspond to the binning of the simulated fluence ($\Phi$). The correction factors estimated via Eq. (3), are presented in Table 2.

**Table 2** Correction factors $f_{par}$ for the scattering of neutrons in the sample and experimental setup, estimated via MCNP6 simulations

| Neutron energy (MeV) | $^{232}$Th | $^{238}$U | $^{235}$U |
|---|---|---|---|
| 2.0 | 0.99 | 0.98 | 0.82 |
| 2.5 | 0.97 | 0.97 | 0.84 |
| 3.0 | 0.97 | 0.96 | 0.84 |
| 3.5 | 0.96 | 0.96 | 0.84 |
| 4.0 | 0.95 | 0.95 | 0.84 |
| 4.3 | 0.95 | 0.95 | 0.83 |
| 4.7 | 0.95 | 0.94 | 0.83 |
| 5.3 | 0.94 | 0.93 | 0.83 |
| 9.9 | 0.90 | 0.88 | 0.79 |
| 14.8 | 0.94 | 0.93 | 0.86 |
| 16.5 | 0.95 | 0.94 | 0.86 |
| 17.8 | 0.95 | 0.94 | 0.86 |

The scattering of the main neutron beam in the experimental area is not included in the simulations. This scattering is expected to slightly increase the low energy part of the simulations [33]. Even a low parasitic flux at low energies can cause a huge effect in the $^{235}$U sample (due to the high cross section at low energies), leaving at the same time the corrections for the $^{232}$Th and $^{238}$U samples unaltered. This can be better understood by comparing the evaluated fission cross sections of $^{232}$Th, $^{238}$U and $^{235}$U from ENDF/B-VIII.0 [32], presented in Fig. 5. As seen in the figure, the $^{235}$U(n,f) cross

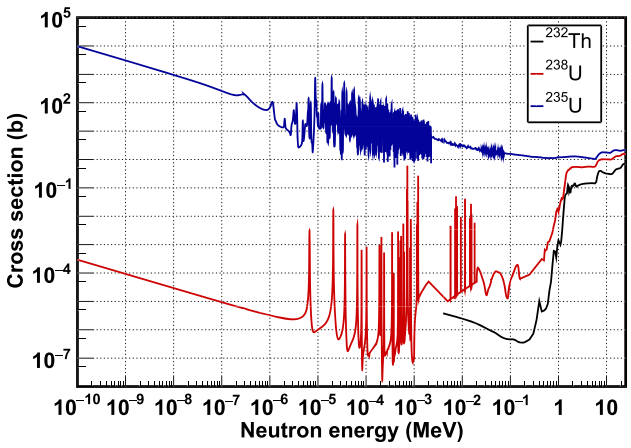


**Fig. 5** Evaluated fission cross sections for $^{232}$Th (black line), $^{238}$U (red line) and $^{235}$U (blue line) taken from ENDF/B-VIII.0 [32]

section at low energies has a value of approximately 8 order of magnitudes higher than the $^{238}$U(n,f) cross section, while there is no evaluation for the $^{232}$Th(n,f) cross section, but it is expected to be very low, lower than the corresponding one of the $^{238}$U sample in the low energy region. In addition, it is interesting to note the similar shape of the $^{232}$Th(n,f) and $^{238}$U(n,f) cross sections up to approximately 6 MeV. The similar slope at the two cross-section thresholds, combined with the low cross-section values in the low energy region is expected to yield a similar response to parasitic neutrons that might be present in the region. This was tested, by artificially adding a low energy parasitic flux in various energy regions of the Monte Carlo simulations, which did not affect the cross-section results of the $^{232}$Th(n,f) reaction estimated using the $^{238}$U sample as reference. In addition, the similar fission cross-section shape of the $^{232}$Th and $^{238}$U samples results in very close values of the correction factors estimated by the Monte Carlo simulations at all neutron energies, as seen in Table 2, while the correction for the $^{235}$U sample is higher for all irradiations.

Another group of parasitic neutrons, created via interactions of the particle beam with nuclei present in the beam line (such as $^{12}$C, $^{16}$O) and in the target container (gas cell and $^{3}$H target holder) was estimated experimentally for the $^{2}$H(d,n) and $^{3}$H(d,n) irradiations, by measurements with and without the presence of the neutron producing target. In the case of the $^{2}$H(d,n) neutron producing reaction, the deuterium gas was removed from the gas cell and the fission counts recorded were attributed to parasitic neutrons from deuteron induced reactions in the beam line and the materials of the gas cell, such as $^{12}$C(d,n), and it was taken into account in the analysis by subtracting the parasitic counts from the total fission counts after normalizing to the incident charge. The contribution from these parasitic neutrons was estimated to be 34%, 33% and 44% for the $^{238}$U, $^{232}$Th and $^{235}$U sample respectively. In the case of the irradiations with the $^{3}$H(d,n), an identical target holder was placed in the beam, where instead of the entrance Mo foils, the TiT target and the Cu on which the target is deposited, a single Cu foil was placed in the position of the target. However, the contribution from these parasitic neutrons was found to be negligible in all cases (less than 1%).

The last group of parasitic neutrons, is related to reactions of the charged particle beam with the materials of the target itself. The most common nuclei found in the target and the target surrounding materials are $^{2}$H implanted from previous irradiations in the TiT target or in the surrounding materials of the gas cell, Ti in the case the TiT target is used and $^{12}$C from carbon built up, due to the unavoidable presence of hydrocarbons in the beam line. The interaction of these nuclei with the charged particle beam can result in (p,n) reactions, as well as (d,n) and (d,np) reactions in the case of the deuteron beam. Previous studies with the time-of-flight technique implementing a pulsed neutron source for the characterization of the quasi-monoenergetic neutron beam produced with a TiT target bombarded by proton [34] and deuteron [31,35] beams at various energies, has shown distinct peaks in the neutron spectra, depending on the energy of the deuteron beam and on the number of times the target was previously used.

In order to estimate the effect of these parasitic neutrons in the final cross-section results, calculations were made to approximate the parasitic peaks present in the fluence from various reactions, taking into account an approximate mass for the nuclei, the fluence of the charged particle beam, estimated via the current integrator and the cross section of each reaction (taken either from the Experimental Nuclear Reaction Data Library EXFOR [5], or from TENDL-2019 [36]). While obtaining an accurate quantitative result was not possible, it was observed that the addition of the parasitic fluence does not affect the final cross-section results of the $^{232}$Th(n,f) cross section calculated with the $^{238}$U(n,f) reaction as reference. It is interesting to note that in the case of the $^{3}$H(p,n) irradiations above 2.5 MeV, the creation of parasitic neutrons from the excited states of the Ti isotopes seems to have an important contribution in the parasitic counts of $^{235}$U and of the $^{237}$Np sample which was used as monitor. However, the cross-section values of the excited states of the Ti isotopes were estimated via EMPIRE calculations [37], so in this case the uncertainty in the parasitic fluence was quite high.

### 3.3 Amplitude cut correction

Monte Carlo simulations were performed with FLUKA [23,24], using the GEF code [38] as fission event generator, for the description of the energy deposition of the fission fragments in the Micromegas detectors. The characteristics of the fission fragments for each actinide sample,

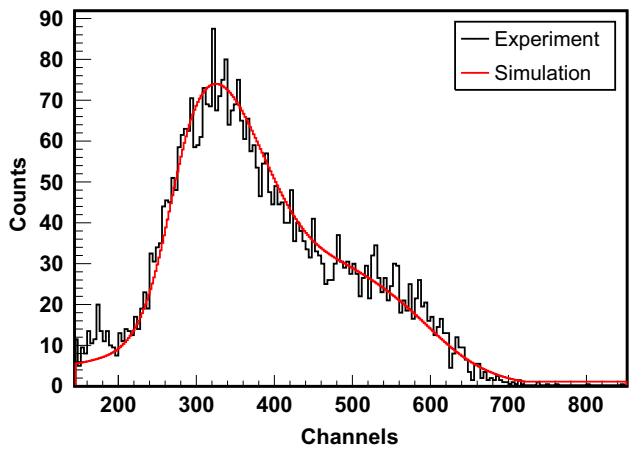


**Fig. 6** Experimental amplitude spectrum (black line) along with the calibrated and convoluted simulated spectrum (red line) for the $^{232}$Th sample

namely their mass and atomic numbers and kinetic energy, are imported from the GEF code in order to describe the source. The emission of the fission fragments is assumed to be isotropic, as a first order approximation, ignoring angular distribution effects above 10 MeV. The output of the FLUKA simulation for each actinide sample, which corresponds to the energy deposited in the gas of the Micromegas detector, is calibrated and then convoluted with a skewed gaussian response function, in order to be compared with the experimental spectra. The comparison between the experimental spectrum and the calibrated and convoluted FLUKA spectrum for the $^{232}$Th sample, is presented in Fig. 6.

The simulations from the FLUKA code were used for the correction of the fission fragments lost under the $\alpha$ peak from the natural radioactivity of the samples present in the experimental spectra. The correction was in the order of 3–5% for all actinide samples. The correction was also estimated by assuming that the energy deposition of the $\alpha$ particles extends linearly to zero. It was estimated that the difference in the final cross-section results, when the correction for the lost fission fragments was calculated with this simple approach and with the FLUKA simulations, was less than 1% in all cases.

### 3.4 Dead time

The dead time of the acquisition system was calculated as the ratio the system was busy with processing a signal (live time) to the acquisition time (real time), according to the equation

$$f_{DT} = \frac{Live\ time}{Real\ time} \tag{4}$$

The dead time of the acquisition system was negligible, since it was estimated to be less than 0.3% for all actinide samples at all neutron energies.

**Table 3** Systematic uncertainties of the $^{232}$Th(n,f) cross section calculation

| Contribution | Uncertainty |
|---|---|
| Parasitic neutrons | 1–2% |
| Amplitude cut | <1% |
| Dead time | <0.1% |
| Neutron fluence | <1% |
| Sample mass | 3% |
| Reference cross section | 1.3–1.5% |

### 3.5 Uncertainties

The statistical uncertainty of the cross-section results for the $^{232}$Th(n,f) reaction is a result of the fission fragment yields from $^{232}$Th sample and the reference ones. The various contributions of the systematic uncertainties in the cross-section results are presented in Table 3.

The uncertainty in the parasitic neutrons correction factor was estimated by multiplying the parasitic tail estimated by the MCNP simulations and by adding the expected parasitic peaks, as discussed in Sect. 3.2. It was estimated that the effect in the final cross-section results was in the order of 1–2% and within the statistical errors. Regarding the amplitude cut correction, it was estimated via the FLUKA simulations and by assuming that the fission fragment counts extend linearly to the end of the amplitude spectra, as presented in Sect. 3.3. The final cross-section results of the $^{232}$Th(n,f) reaction varied less than 1% with the different methods for the amplitude cut correction. The systematic uncertainty from the dead time was negligible, since this correction was very small in all cases. The uncertainty in the neutron fluence is a result of the geometrical correction, due to the different positions of the samples with respect to the neutron beam. In the case of the irradiations with the $^{3}$H(p,n) and with the $^{3}$H(d,n) reactions this correction is negligible, because the $^{232}$Th samples were placed in contact with the reference samples. For the $^{2}$H(d,n) irradiation the uncertainty was estimated via the comparison of the $^{238}$U samples, placed on both sides of the $^{232}$Th sample, and was found to be less than 1%.The systematic uncertainty in the sample mass was in the order of 3%, while the statistical uncertainty was less than 1% for all actinide samples, as mentioned in Sect. 2.2. Finally, the uncertainty in the evaluated cross sections of the reference samples $^{238}$U and $^{235}$U was 1.3–1.5% [39].

## 4 Results

The fission cross-section results for $^{232}$Th, obtained by the analysis presented in Sect. 3 are presented in Table 4 along with their statistical uncertainties. The $^{238}$U(n,f) reaction was

**Table 4** Cross-section results for the $^{232}$Th(n,f) reaction with their statistical uncertainties

| Neutron energy (MeV) | Cross section (b) |
|---|---|
| 2.0 ± 0.1 | 0.117 ± 0.005 |
| 2.5 ± 0.1 | 0.112 ± 0.003 |
| 3.0 ± 0.1 | 0.135 ± 0.004 |
| 3.5 ± 0.1 | 0.137 ± 0.004 |
| 4.0 ± 0.1 | 0.142 ± 0.004 |
| 4.3 ± 0.1 | 0.137 ± 0.004 |
| 4.7 ± 0.1 | 0.147 ± 0.004 |
| 5.3 ± 0.1 | 0.135 ± 0.004 |
| 9.9 ± 0.1 | 0.304 ± 0.005 |
| 14.8 ± 0.5 | 0.383 ± 0.023 |
| 16.5 ± 0.5 | 0.456 ± 0.018 |
| 17.8 ± 0.3 | 0.50 ± 0.04 |

used as reference for the cross section calculation at all neutron energies, while the $^{235}$U(n,f) was used in addition for the 2.0 and 2.5 MeV irradiations (at higher neutron energies there was a significant contribution from parasitic neutrons to the fission counts of the $^{235}$U sample, preventing from using it as a reference). In the latter case the cross-section was estimated as the average cross-section value of the two reference samples, with the difference between them being less than 1% for both neutron energies. The systematic uncertainties are presented in Table 3. The comparison between the data of this work and the experimental data found in EXFOR [5], along with the latest evaluated libraries ENDF/B-VIII.0 [32], JEFF-3.3 [40], JENDL-4.0 [41] and CENDL-3.2 [42] is presented in Fig. 7.

Regarding the results in the energy region 2.0–5.3 MeV, presented in Fig. 7a, a very good agreement is observed between the data of the present work and the data of Blons et al. [10,12] and Muir and Veeser [14], while there is an overall agreement with the data of Lisowksi et al. [7], D'hondt et al. [11], Casanova and Valle [13], Kalinin and Pankratov [20] and Henkel [21]. However, the data of D'hondt and Casanova and Valle have uncertainties equal to 16.7% and 15.4% respectively, while no uncertainties for the data of Kalinin and Pankratov are given in EXFOR. The most recent data of Shcherbakov et al. [6] are in fair agreement with the data of Meadows [9] and seem to give slightly higher cross-section values than the data of the present work, even though an agreement within errors is observed for the neutron energies at 3.0, 3.5 and 4.5 MeV. Finally, the data of Ermagambetov et al. [16] have systematically lower cross-section values compared to the data of the present work. The cross-section results of our work are in overall good agreement with the ENDF/B-VIII.0 (which agrees with JEFF-3.3) evaluation, while the JENDL-4.0 and CENDL-3.2 evaluations seem to have slightly higher cross-section values.

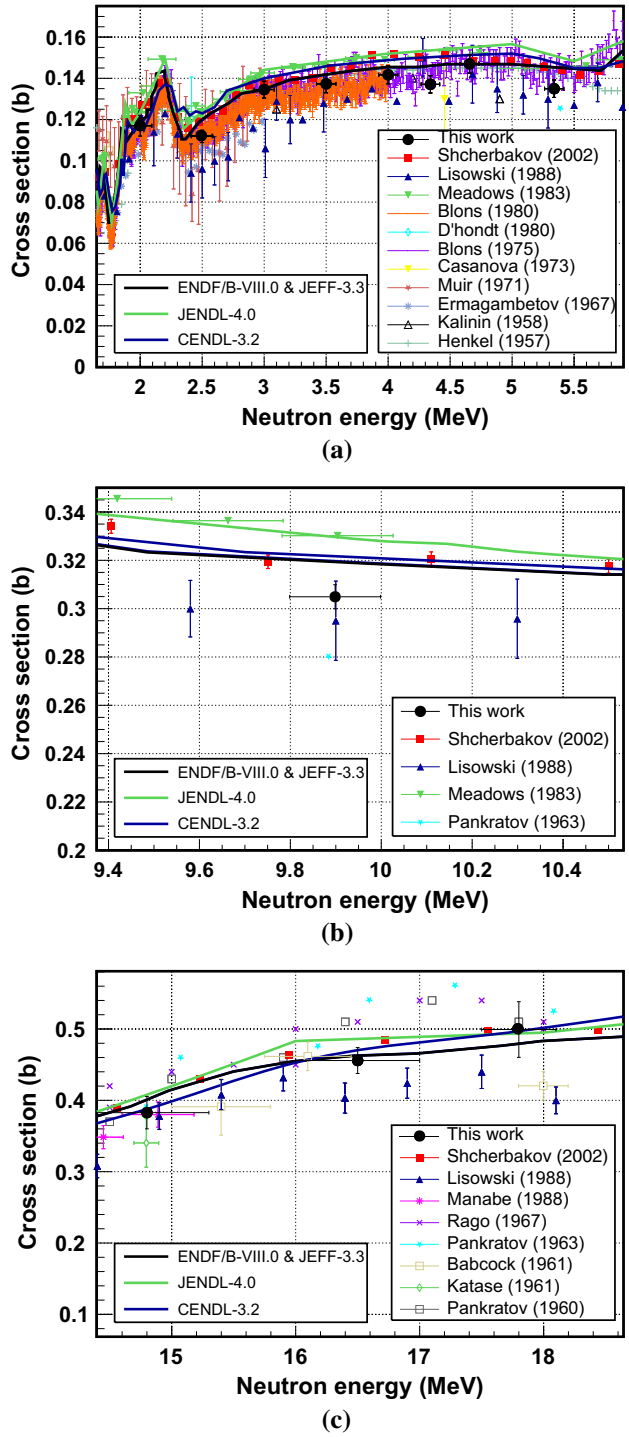


**Fig. 7** Cross-section results from this work (black points) along with the experimental data available in EXFOR [5] and the latest evaluated libraries ENDF/B-VIII.0 [32] (which agrees with JEFF-3.3 [40]) (black line), JENDL-4.0 [41] (green line) and CENDL-3.2 [42] (blue line) at **a** the energy region from 2.0 to 5.3 MeV, **b** 9.9 MeV and **c** at the energy region from 14.8 to 17.8 MeV

For the data point at 9.9 MeV, presented in Fig. 7b, an agreement within errors is observed with the point of Lisowksi et al. at a slightly higher energy, while the data of Shcherbakov et al. and Meadows have higher cross-section values. One point of Pankratov [17] in this energy region has a lower cross-section value than the one determined in the present work. Regarding the latest evaluations, all overestimate the present cross-section values, with the ENDF/B-VIII.0 (which agrees with JEFF-3.3) being closer to this data point, having a 5% difference in the cross-section value.

In the higher energy region the cross-section results are presented in Fig. 7c. As seen in the figure, they are in agreement within uncertainties with the available data in EXFOR for the energy points at 14.8 MeV and 17.8 MeV. Very good agreement is observed at 14.8 MeV with the points of Pankratov, Manabe et al. [8] and Lisowski et al., while the point from Katase [18], even though in agreement within errors with the present work, has a lower cross-section value and 10% uncertainty. At 17.8 MeV the data point is in excellent agreement with the point from Pankratov et al. [19], the only one in the same energy as the present work. The cross-section point at 16.5 MeV is in between the latest data of Shcherbakov et al. and Lisowksi et al. and in agreement within error with the point of Babcock [5] at a lower energy, while the points from Rago and Goldstein [15], Pankratov and Pankratov et al. have higher cross-section values. In this energy region the data points from this work are in better agreement with the CENDL-3.2 library, while agreement within errors is also seen with the ENDF/B-VIII.0 (which agrees with JEFF-3.3) at all data points.

The only data covering the whole fast neutron energy region are the latest datasets of Shcherbakov et al. and the data of Lisowksi et al. Overall good agreement is observed with these specific datasets, since agreement within errors is observed for the majority of the data points. The data from Shcherbakov et al. have systematically higher cross-section values than the data of Lisowksi et al., while the data of the present work seem to be in the middle of these datasets. For energies higher than 16 MeV, namely the last two cross-section points, the data of this work are in better agreement with the data from Shcherbakov et al. Regarding the latest evaluated libraries, overall best agreement is observed with the latest ENDF/B-VIII.0 evaluation (which agrees with JEFF-3.3).

## 5 Conclusions

The neutron induced fission of $^{232}$Th was measured at the 5.5 MV Van de Graaff Tandem accelerator in the National Centre for Scientific Research "Demokritos" with Micromegas detectors, using quasi-monoenergetic neutron beams at fast neutron energies, produced via the $^{3}$H(p,n), $^{2}$H(d,n) and $^{3}$H(d,n) reactions.

The cross-section results are in very good agreement with the latest evaluations and certain experimental datasets in literature and demonstrate that quasi-monoenergetic neutron beams can provide accurate results over a broad energy range and resolve existing discrepancies, even in the absence of time-of-flight capabilities, provided that all the experimental details are thoroughly investigated. Special attention was given to the study of the parasitic neutrons produced from neutron scattering in the experimental area and experimental setup and via charged particle reactions of the particle beam with the beam line and the neutron producing target. Due to the similar fission cross section of $^{232}$Th and $^{238}$U it was confirmed that the contribution from these parasitic neutrons to the final cross-section results was negligible.

**Acknowledgements** This research is implemented through IKY scholarships program and co-financed by the European Union (European Social Fund –ESF) and Greek national funds through the action entitled "Reinforcement of Postdoctoral Researchers -2nd call (MIS 5033021)", in the framework of the Operational Programme "Human Resources Development Program, Education and Lifelong Learning" of the National Strategic Reference Framework.
We acknowledge support of this work by the project CALIBRA/EYIE (MIS 5002799), which is implemented under the Action "Reinforcement of the Research and Innovation Infrastructures", funded by the Operational Program "Competitiveness, Entrepreneurship and Innovation" (NSRF 2014-2020) and co-financed by Greece and the European Union (European Regional Development Fund).

**Funding** Open Access funding provided by CERN.

**Data availability statement** This manuscript has no associated data or the data will not be deposited. [Authors' comment: The results from this work will be deposited at the Experimental Nuclear Reaction Data (EXFOR) database.]

**Open Access** This article is licensed under a Creative Commons Attribution 4.0 International License, which permits use, sharing, adaptation, distribution and reproduction in any medium or format, as long as you give appropriate credit to the original author(s) and the source, provide a link to the Creative Commons licence, and indicate if changes were made. The images or other third party material in this article are included in the article's Creative Commons licence, unless indicated otherwise in a credit line to the material. If material is not included in the article's Creative Commons licence and your intended use is not permitted by statutory regulation or exceeds the permitted use, you will need to obtain permission directly from the copyright holder. To view a copy of this licence, visit http://creativecommons.org/licenses/by/4.0/.

## References

1. D. Greneche, M. Chhor, in *Development of the thorium fuel cycle*. ed. by I. Crossland (Woodhead Publishing, Sawston, 2012), p. 177
2. International Atomic Energy Agency (IAEA), Thorium fuel cycle – Potential benefits and challenges. (IAEA-TECDOC-1450, 2005), https://www-pub.iaea.org/MTCD/Publications/PDF/TE_1450_web.pdf. Accessed 19 Jul 2021

3. P. Möller, J. Nix, *Calculation of Fission Barriers, (Proceedings of the Third IAEA Symposium on the Physics and Chemistry of Fission)* (Rochester, New York, 1974), p. 103
4. M. Sin, R. Capote, A. Ventura, M. Herman, P. Obložinsky, Phys. Rev. C **74**, 014608 (2006). https://doi.org/10.1103/PhysRevC.74.014608
5. V.V. Zerkin, B. Pritychenko, Nucl. Instrum. Methods A **888**(31), 10 (2018)
6. O. Shcherbakov et al., J. Nucl. Sci. Technol. **39**(sup2), 230 (2002). https://doi.org/10.1080/00223131.2002.10875081
7. P.W. Lisowski et al., in Neutron induced fission cross section ratios for $^{232}$Th, $^{235,238}$U, $^{237}$Np and $^{239}$Pu from 1 to 400 MeV, (Proc. Int. Conf. Nuclear Data for Science and Technology, Mito, Japan, May 30–June, 1988), p. 97
8. F. Manabe, Technol. Reports Tohoku Univ. **52**, 97 (1988)
9. J.W. Meadows, Techn. Rep. **No. ANL/NDM-83**(1983)
10. J. Blons, C. Mazur, D. Paya, M. Ribrag, H. Weigmann, *Proc* (Int, Winter Meeting on Nuclear Physics, 1980)
11. P. D'hondt, C. Wagemans, G. Barreau, A.J. Deruytter, Ann. Nucl. Energy **7**, 367 (1980)
12. J. Blons, C. Mazur, D. Paya, Phys. Rev. Lett. **35**(1749), 10 (1975)
13. J. Casanova, J. Valle, A. Fís. **69**, 71 (1973)
14. D.W. Muir, L.R. Veeser, Proc. , Third Conf. on nuclear cross sections and technology. Knoxville **1**, 292 (1971)
15. P.F. Rago, N. Goldstein, Health Phys. **13**, 654 (1967)
16. S.B. Ermagambetov, V.F. Kuznetsov, G.N. Smirenkin, Yad. Fiz. **5**, 257 (1967) **14**(2), 177 (1963)
17. V.M. Pankratov, Atom. Energ. **14**(2), 177 (1963)
18. A. Katase, *Data Published in the Memoirs of the Faculty of Engineering*, vol. 23 (Kyushu University, Fukuoka, 1961), p. 81
19. V.M. Pankratov, N.A. Vlasov, B.V. Rybakov, Atom. Energ. **9**, 399 (1960)
20. S.P. Kalinin, V.M. Pankratov, Second Internat. Atom. Eng. Conf. **16**, 136(2149) (1958)
21. R.L. Henkel, Second Internat. Los Alamos Scientific Lab. Reports No. **2122**(1957)
22. R. Whitcher, Radiat. Prot. Dosim. **118**, 459 (2006). https://doi.org/10.1093/rpd/nci381
23. G. Battistoni et al., AIP Conf. Proc. **896**, 31 (2007)
24. T.T. Böhlen et al., Nucl. Data Sheets **120**(211), 10 (2014)
25. F. James, MINUIT - Function Minimization and Error Analysis (Version 94.1). (CERN Program Library entry D506, Geneva, 1998), https://inspirehep.net/files/6dc93850d19776251caffa506d4e7c27. Accessed 19 July 2021
26. A. Stamatopoulos et al., Eur. Phys. J. A **54**(7), 10 (2018)
27. M. Diakaki et al., Eur. Phys. J. A **49**(62), 10 (2013)
28. Y. Giomataris, Nucl. Instrum. Methods A **419**, 239 (1998)
29. S. Andriamonje et al., J. Korean Phys. Soc. **59**, 1597 (2011). https://doi.org/10.3938/jkps.59.1601
30. J. Armstrong et al., ed. C.J. Werner, MCNP Users Manual - Code Version 6.2, (LA-UR-17-29981, 2017)
31. D.L. Smith, A.J.M. Plompen, V. Semkova, in Correction for low energy neutrons by spectral indexing, (A report by the working party on international evaluation co-operation of the NEA nuclear science committee, ISBN 92-64-01070-X, NEA/WPEC-19, 2005), p. 155
32. D.A. Brown et al., Nucl. Data Sheets (2018). https://doi.org/10.1016/j.nds.2018.02.001
33. M. Diakaki et al., EPJ Web Conf. **239**, 05001 (2020). https://doi.org/10.1051/epjconf/202023905001
34. S.P. Simakov, G.N. Lovchikova, A.M. Trufanov, V.A. Vinogradov, M.G. Kobozev, Proceedings of XIV International Workshop on Nuclear Fission. Physics **164**(2000)
35. A. Fessler, A.J.M. Plompen, D.L. Smith, J.W. Meadows, Y. Ikeda, Nucl. Sci. Eng. **134**, 171 (2000). https://doi.org/10.13182/NSE99-14
36. A.J. Koning et al., Nucl. Data Sheets **155**, 1 (2019). https://doi.org/10.1016/j.nds.2019.01.002
37. M. Herman et al., Nucl. Data Sheets **108**, 2655 (2007). https://doi.org/10.1016/j.nds.2007.11.003
38. K.-H. Schmidt, B. Jurado, C. Amouroux, C. Schmitt, Nucl. Data Sheets **131**, 107 (2016). https://doi.org/10.1016/j.nds.2015.12.009
39. A.D. Carlson et al., Nucl. Data Sheets **148**, 143 (2018). https://doi.org/10.1016/j.nds.2018.02.002
40. A. Plompen et al., Eur. Phys. J. A **56**(143), 10 (2020.1140/epja/s10050-020-00141-9.)
41. K. Shibata et al., J. Nucl. Sci. Technol. (2011). https://doi.org/10.1080/18811248.2011.9711675
42. Z. Ge et al., EPJ Web Conf. **239**, 09001 (2020). https://doi.org/10.1051/epjconf/202023909001